Multichannel study on the fragmentation of the $1g_{9/2}$ isobaric analog resonance in ^{53}Mn

J. Sziklai
Central Research Institute for Physics, Budapest 114, P.O. Box 49, Hungary H-1525

J. A. Cameron
Tandem Accelerator Laboratory, McMaster University, Hamilton, Ontario, Canada L8S 4K1

I. M. Szöghy
Département de Physique, Université Laval, Québec City, Québec, Canada G1K 7P4

T. Vass*
Rutgers University, Physics Department, Box 849, Piscataway, New Jersey 08855
(Received 17 November 1992; revised manuscript received 20 September 1993)

Fragments of the $1g_{9/2}$ isobaric analog resonance in ^{53}Mn corresponding to the 3.715 MeV state ($S_n = 0.57$) in ^{53}Cr were located using the ^{52}Cr(p,p_0), ^{52}Cr(p,p_1), ^{52}Cr$(p,p_1\gamma)$, ^{52}Cr$(p,p_2\gamma)$, and ^{52}Cr$(p,\gamma)^{53}$Mn reactions. Differential cross sections were measured in the 4.06–4.28 MeV, and the γ-excitation curves in the 4.04–4.35 MeV proton energy region. Spins, parities, and partial widths were determined with the aid of R-matrix analysis for all resonances observed in the region. The spins of the $1g_{9/2}$ resonance fragments were found independently from $(p,p_1\gamma)$, $(p,p_2\gamma)$, and (p,γ) angular distribution measurements and their analyses. Nineteen fragments were identified and their γ-branching ratios to low lying levels of ^{53}Mn were also deduced. Partial widths for each fragment in all four channels were derived. Channel-channel correlations were calculated. Fine structure analyses were carried out in all open channels. Inelastic spectroscopic factors and Coulomb displacement energy for the $1g_{9/2}$ state were also derived.

PACS number(s): 24.30.Gd, 21.10.Jx, 25.40.−h, 27.40.+z

I. INTRODUCTION

The $1g_{9/2}$ isobaric analog resonance (IAR) of the E_x=3.715 MeV ($S_n = 0.57$) $1g_{9/2}$ parent state [1] in ^{53}Mn was studied by several authors [2–10]. It was shown by Galè *et al.* [6,7] and Fodor *et al.* [8,9] that, in spite of the very limited energy resolutions they applied, this $1g_{9/2}$ IAR was found fragmented. To get more information on the fragmentation and fine structure of this IAR, experiments with better resolution were required. Based on an earlier study on the fragmentations of the $1g_{9/2}$ IARs in the ^{50}Cr+p system [11], the ^{52}Cr$(p,\gamma)^{53}$Mn, ^{52}Cr$(p,p_1\gamma)$, and ^{52}Cr$(p,p_2\gamma)$ reactions were used to select all possible fragments of this IAR, yielding 24 candidates [12]. Ozawa *et al.* [13] published a high-resolution study on analog states in ^{53}Mn. However, from their R-matrix analysis, only one $1g_{9/2}$ fragment was identified in the energy range of this $1g_{9/2}$ IAR. Its single-particle strength accounts for only a small portion of the strength corresonding to the large spectroscopic factor of the parent state. In order to clear up the disagreements between the papers cited differential cross sections for the ^{52}Cr(p,p_0) and ^{52}Cr(p,p_1) (see Fig. 1) reactions in the bombarding energy region of E_p = 4.06–4.28 MeV were measured. This way the complete open channel study of this IAR became possible. Our aim was to find all fragments in all the open channels as well, and based on their fine structure analysis compare the characteristics of the deduced strength functions in the different channels. This will enable us to study the fine structure as a multichannel phenomena. To achieve this task the study of the ^{52}Cr(p,γ), ^{52}Cr$(p,p_1\gamma)$, and ^{52}Cr$(p,p_2\gamma)$ reactions was also completed.

II. EXPERIMENTAL PROCEDURE

The proton scattering experiments were carried out with the proton beam of the 7.5 MV Van de Graaff accelerator of Laval University where, by placing stringent geometrical limitations on the beam, an oveall resolution of $\sim$ 600 eV was achieved. A beam current of $\sim$ 1.5 μA was used and 400 mC charges were accumulated per point to have good statistical accuracy. The excitation curve was measured in energy steps of $\sim$ 300 eV. The beam energy calibration was obtained by reproducing the well-known $1g_{9/2}$ IAR in ^{59}Cu at 3.547 MeV proton bombarding energy. Absolute energies are considered accurate to ±2 keV. The relative energies over a small proton bombarding energy range were reproducible to a few hundred eV.

*Permanent address: Central Research Institute for Physics, Budapest 114, P.O. Box 49, Hungary H-1525.

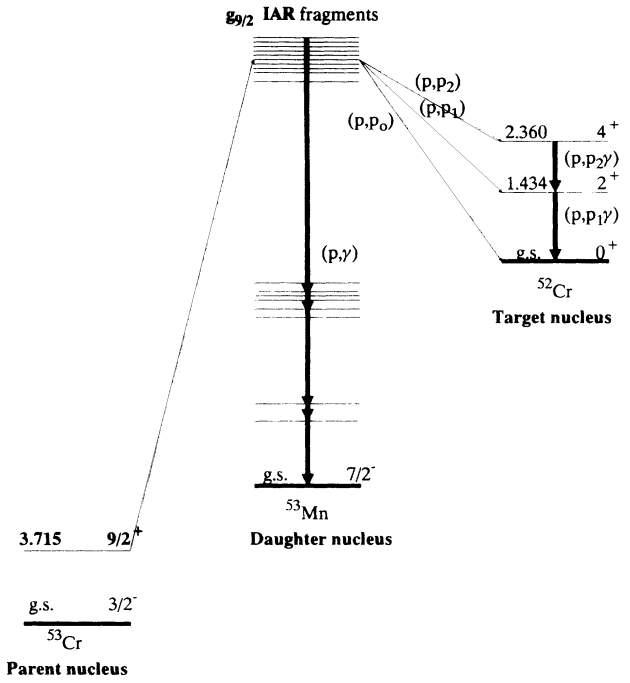

FIG. 1. Schematics of the reactions studied.

The thin targets for the scattering experiments were prepared by evaporating isotopically enriched (98.8%) $^{52}Cr_2O_3$ onto 5 and 10 $\mu g/cm^2$ thick carbon foil backings. The target thickness was about 5 $\mu g/cm^2$. The beam entered a scattering chamber of 40 cm radius after an adjustable collimator system in order to produce a beam spot of less than 1 mm in diameter. Six Ortec surface barrier detectors detected the elastically and inelastically scattered protons simultaneously at laboratory angles of 90°, 105°, 125°, 135°, 145°, and 165° to the beam. To ensure the correspondence of the resonances found in $(p,p_1\gamma)$ and (p,γ) experiments, an Ortec Gamma-X detector (with a relative efficiency of 26% for the 1.333 MeV ^{60}Co line) was placed at −90° and simultaneous γ-spectra were also measured. The singles spectra were collected by a PDP-15 on-line computer with seven 4096 channel Canberra analog to digital converters and recorded onto magtape for later analysis.

The experiments involving γ rays were carried out with the proton beam of the FN Tandem Accelerator of McMaster University where the spiral-inclined-field acclerator tubes by Dowlish, and the NEC pelletron charging system, together with the optical fast-feedback terminal stabilizer, made it possible to keep the overall energy resolution at $\leq$ 700 eV, even for extended runs. This was essential for the γ-capture studies, since the partial widths in these channels are several orders of magnitude weaker than those of the particle channels.

The targets for the γ-ray studies were prepared by evaporating isotopically enriched (98.8%) $^{52}Cr_2O_3$ onto thick, previously vacuum-degassed tungsten backings. The target thickness was about 11 $\mu g/cm^2$. Degassed tungsten was also used for beam collimators and for lining the small target chamber with diameter of 5 cm. The use of degassed tungsten enabled us to collect γ spectra with negligible fluorine contamination. A target current of 1.5 μA was used. A cool trap in front of the target chamber helped to prevent contaminant depositions on the beam spot.

The γ rays were detected by two Ortec Gamma-X detectors. One with 29% efficiency and 1.68 keV resolution for the 1.333 MeV ^{60}Co line, was used at 55° to the beam for the excitation function measurements and in the 90°-45°-0°-60°-30° cycles as moving detector in the angular distribution measurements. The other, with 23% efficiency and 1.78 keV resolution, was used at −90° as a monitor. Both detectors had extremely good resolution at high γ-ray energies as well, i.e., 6.5 and 7.0 keV at 10.670 MeV.

The γ spectra were collected by a Tracor Northern TN-1710 multichannel analyzer and transferred via a serial line to a VAX 11/750 computer for on line inspection and later analysis.

The γ excitation functions were measured in 1.3 keV steps. The collected charge was 600 μC per point for the excitation function measurements, while for the γ angular distribution measurements collected charges from 1.2 to 12 mC per angle were used.

III. RESULTS

A. Proton scattering differential cross sections and the *R*-matrix analysis

Our main interest was to find the $l = 4$ $1g_{9/2}$ fragments. However, due to the low penetrabilities for the higher orbital momenta, the (p,p_0) and (p,p_1) reactions are mainly sensitive to resonances with $l \leq 2$. The positions of the candidates of the $1g_{9/2}$ IAR fragments were known from a previous study [12] where reactions sensitive to higher spin resonances [11] were used. The behavior of the inelastic differential cross sections was also helpful in indentifying the $1g_{9/2}$ fragments. The angular distribution for the inelastically scattered protons, originating from an $l = 4$ resonance, rises sharply at back angles, especially at 165°.

Previous $(p,p_1\gamma)$ angular distribution results [12] also helped in deciding on the spins of different $l = 1$ and $l = 2$ resonances, since from the shapes of the resonances in the elastic excitation functions at different angles one can infer the l values of the resonances, but not their spins.

The measured differential cross sections for the elastic and the inelastic scattering to the first excited state (1.4336 MeV, $J^\pi = 2^+$) in ^{52}Cr are shown as points in Figs. 2(a) and 2(b). These excitation functions were analyzed with the multilevel multichannel R-matrix code [14] MULTI and the analysis of the inelastic data was performed concurrently with the analysis of the elastic data. Table I shows the resonance spins, orbital momenta, and channel spins considered throughout the analyses. The $l' = 0$, $l' = 1$, and $l' = 2$ resonances can decay with two different channel spins to the inelastic channel. For the $J_R = \frac{1}{2}$ spin resonances it was assumed that the contributions from both channel spins are the same.

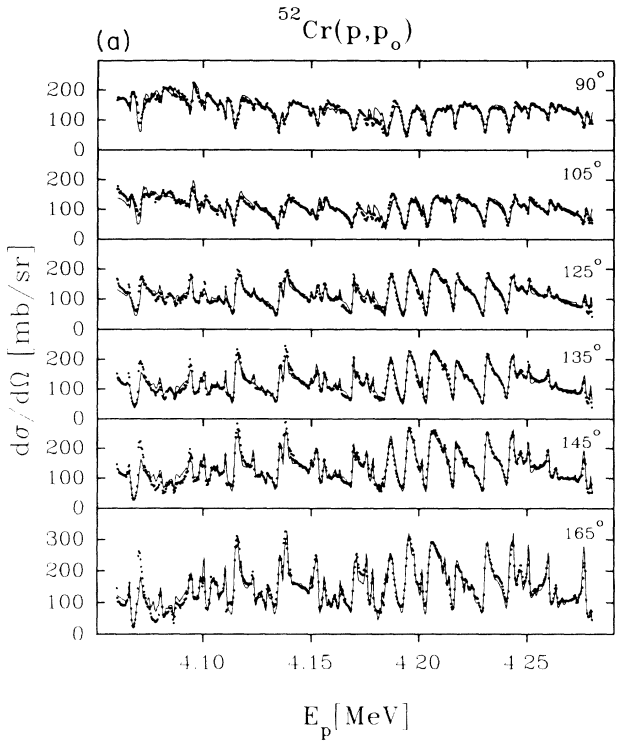

FIG. 2. (a) Differential cross sections for the ^{52}Cr(p,p_0) reaction at lab angles of 90°, 105°, 125°, 135°, 145°, and 165°. The solid lines are the fits to the data calclated by MULTI. (b) Differential cross sections for the ^{52}Cr(p,p_1) reaction at lab angles of 90°, 105°, 125°, 135°, 145°, and 165°. The solid lines are the fits to the data calculated by MULTI.

TABLE I. Resonance spins, orbital momenta, and channel spins considered in the R-matrix analyses of the (p,p_0) and (p,p_1) reactions.

J_R^π	l	l'	s'
$\frac{1}{2}^+$	0	0	$\frac{1}{2}$
		2	$\frac{3}{2}$ $\frac{5}{2}$
$\frac{1}{2}^-$	1	1	$\frac{1}{2}$ $\frac{3}{2}$
$\frac{3}{2}^-$	1	1	$\frac{1}{2}$ $\frac{3}{2}$
$\frac{3}{2}^+$	2	2	$\frac{1}{2}$
		0	$\frac{3}{2}$
		2	$\frac{3}{2}$ $\frac{5}{2}$
$\frac{5}{2}^+$	2	2	$\frac{1}{2}$
		0	$\frac{5}{2}$
		2	$\frac{3}{2}$ $\frac{5}{2}$
$\frac{5}{2}^-$	3	3	$\frac{1}{2}$
		1	$\frac{5}{2}$
$\frac{9}{2}^+$	4	4	$\frac{1}{2}$
		2	$\frac{5}{2}$

For resonances with other spins the channel spin mixture was adjusted to give the best fit. The fitted cross sections are represented by the solid lines in Figs. 2(a) and 2(b). The extensive table of the extracted resonance parameters of all 171 resonances obtained by the R-matrix analyses are deposited in the Physics Auxiliary Publication Service [15].

The cross sections calculated by MULTI were convoluted with a resolution function to simulate energy loss in the target and the other factors which degrade resolution. The applied resolution function consisted of a Lorentzian leading edge curve with a trailing Gaussian edge, and it was specified by the Gaussian full width at half maximum (FWHM) and the ratio of the Lorentzian FWHM to the Gaussian FWHM. These quantities were determined by fitting some very small resonances in the inelastic decay channel possessing total widths much smaller than the resolution function, for which the observed shapes were essentially just the resolution function. This resolution was kept constant while fitting a region of data.

The general fitting procedure consisted of calculating the differential cross sections for a set of resonance parameters, comparing this fit visually with the data, then

adjusting the resonance parameters and recalculating the cross sections until a satisfactory fit was obtained. The resonance parameters adjusted included the resonance energy, angular momentum, and the magnitudes of the width amplitudes for the allowed values of channel spin and orbital angular momentum (see Table I).

At these bombarding energies, the background in the elastic cross sections is largely due to the resonances in the region. Normalizing the data to the fit leads to normalizations which are often strongly dependent on the resonance parameters utilized in a particular fit. Only after a resonably good fit for all of the larger resonances was found, could the smaller resonances be fitted.

B. γ-excitation functions

The excitation functions measured in the 4.04–4.35 MeV proton bombarding energy region are given in Fig. 3. Figure 3(a) shows the excitation function of the ^{52}Cr$(p,p_1\gamma)$ reaction. Several intense resonance around 4.17 MeV show the presence of the $1g_{9/2}$ IAR in this channel. However, one must take into account that other resonaces with spins of 1/2 to 7/2 are also expected to populate the first excited 2^+ state in ^{52}Cr. Figure 3(b) shows the excitation function of the ^{52}Cr$(p,p_2\gamma)$ reaction having the simplest structure among the curves of Fig. 3. The background is very low and only a few stronger resonances, centered around 4.17 MeV appear. Using the same consideration based on penetrabilities (see Fig. 4) for inelastically scattered protons of different orbital momenta as in Ref. [11], it can be expected that all of the $1g_{9/2}$ fragments would appear in this excitation function. For the same reason, $l = 3$ $(5/2^-)$ levels might also contribute to this curve, while no $5/2^+$ resonances would be expected to populate the 4^+ state. Figure 3(c) shows the excitation function of the ground-state γ decay. The ground state has $7/2^-$ spin-parity and a large single-particle strength, thus only resonances of spins $5/2 \leq J_R \leq 9/2$, and possessing some single-particle character appear in this curve, since isospin selection rules forbid $\Delta L = 2$ isovector γ transitions [16]. Figure 3(d) shows the integral excitation function for 2.2 MeV $\leq E_\gamma \leq$ 4.2 MeV. This is the region where the possible analog-to-antianalog transition was expected to appear. According to Ref. [6] some important $1g_{9/2}$ single-particle strengths are located around the proton emission threshold. The main component at $E_x = 6.5$ MeV

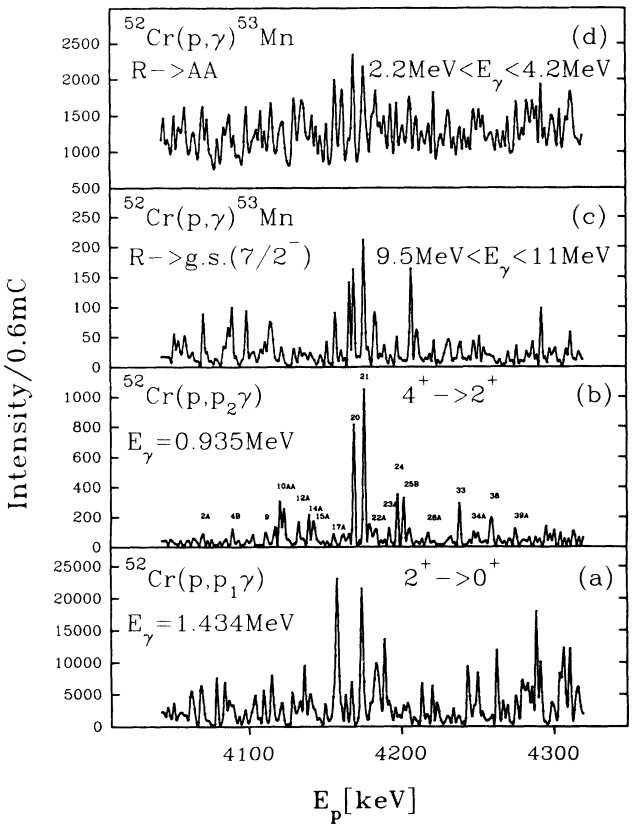

FIG. 3. Excitation functions for the ^{52}Cr$(p,p_1\gamma)$, ^{52}Cr$(p,p_2\gamma)$, ^{52}Cr$(p,\gamma)^{53}$Mn reactions in the proton bombarding energy region of E_p = 4.04–4.35 MeV, measured in 1.3 keV steps.

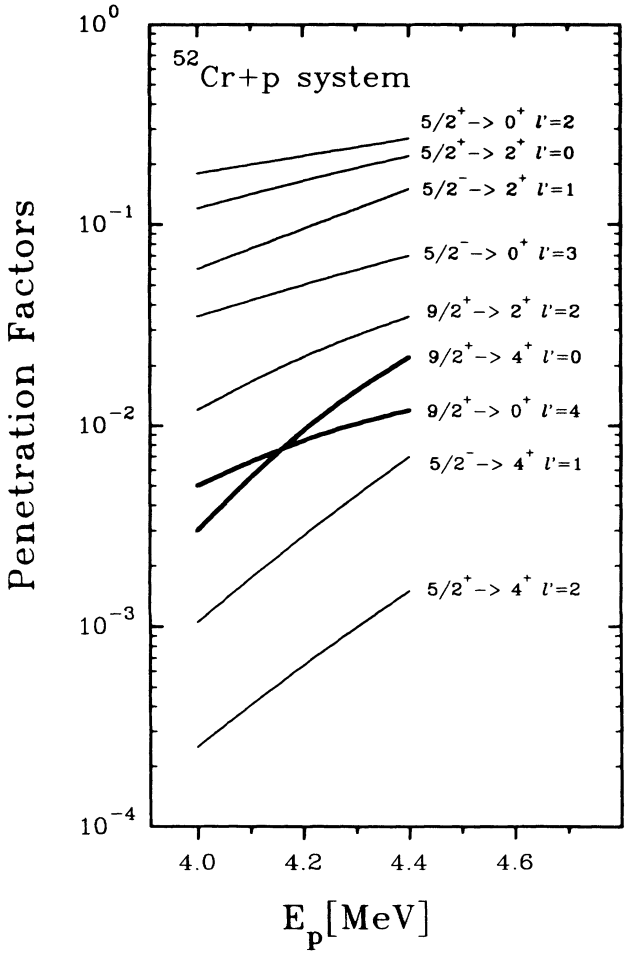

FIG. 4. Penetration factors vs proton bombarding energy for the ^{52}Cr(p,p_0), ^{52}Cr(p,p_1), and ^{52}Cr(p,p_2) reactions. The penetration factors for the (p,p_0) and (p,p_2) reactions are in the same range (bold lines) for the $9/2^+$ resonances.

(S_p = 0.42) was considered as the possible antianalog state. Thus the primary γ rays from the $1g_{9/2}$ IAR fragments were expected to appear in this excitation curve. The structure of this curve is rather complex due to the relatively low energy of the γ rays contributing to this window. In addition to the primary γ rays, secondary transitions originating from non-$g_{9/2}$ resonances also appear. There are, however, some significant correlations with other channels like the $(p, p_2\gamma)$ and (p, γ_0) where all the $1g_{9/2}$ IAR fragments appeared.

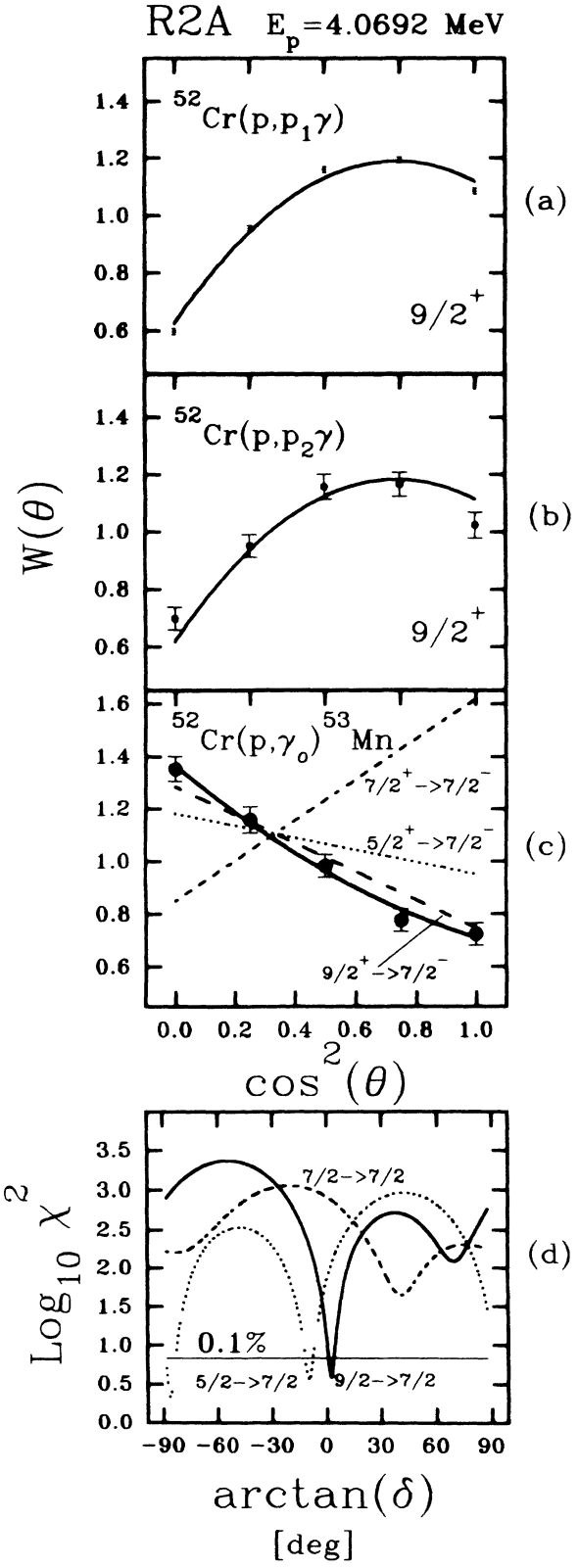

FIG. 5. The angular distributions measured at resonance R2A and their analyses for the (a) ^{52}Cr$(p, p_1\gamma)$, ^{52}Cr$(p, p_2\gamma)$ reactions and the (c) ^{52}Cr$(p, \gamma_0)^{53}$Mn reaction and (d) its χ^2 analysis. In (c) the solid line represents the free 3-parameter fit to the experimental points. The dotted and dashed lines show the 1-parameter fits with different resonance spin assumptions. (For details see Ref. [11].) The χ^2 curves in (d) show that both the $5/2 \rightarrow 7/2$ and the $9/2 \rightarrow 7/2$ transitions satisfy the 0.1% confidence limit. Thus the (p, γ_0) angular distribution *alone* cannot select the real resonance spin. However, considering the angular distributions in (a) and (b) one can safely accept the $9/2^+$ spin parity assignment.

C. γ-angular distributions and resonance spins

In order to determine the spins of the resonances appearing in the excitation functions, the angular distributions of the E_γ=1.4335 MeV γ ray of the ^{52}Cr$(p, p_1\gamma)$ reaction and the E_γ=0.935 MeV γ ray of the ^{52}Cr$(p, p_2\gamma)$ reaction were used. In cases when the measured yields of the ^{52}Cr(p,γ)^{53}Mn reaction were statistically sufficient, their angular distributions were also measured and their χ^2 analyses were carried out. To select the real fragments of the $1g_{9/2}$ IAR from the 24 candidates [12] it was required that the 9/2 spin assignments should agree in all examined channels, including the elastic and inelastic scattering channels. Figures 5–14 show the results of the angular distribution measurements and their analyses for the identified $1g_{9/2}$ resonance fragments in the ^{52}Cr$(p, \gamma)^{53}$Mn, ^{52}Cr$(p, p_1\gamma)$, and ^{52}Cr$(p, p_2\gamma)$ reaction channels. Figure 15 shows the angular distributions for resonances where only the $(p, p_1\gamma)$ and $(p, p_2\gamma)$ angular distributions were measured and analyzed. For cases when the measured $(p, p_1\gamma)$ and $(p, p_2\gamma)$ angular distributions contained the effects of close-lying, lower-spin interfering resonances [see Figs. 6(a), 8(a), 9(a), 10(a), 14(a), and 15], to determine the yields originating from the 9/2 resonances, the method of normalized angular distributions was used. This method is based on that assumption that the measured angular distribution originates, e.g., from two resonances with different spins and is fitted with the *incoherent* sum of the two angular distributions with assumed resonance spins, since the outgoing protons *were not observed.* The fitted parameters in this case are the amplitude and the ratio of the intensities of the two components. Details of this method are given in Ref. [11].

D. γ-branching ratios of the $9/2^+$ IAR fragments

Figure 16 shows the decay scheme and the branching ratios for the primary γ transitions from the fragments

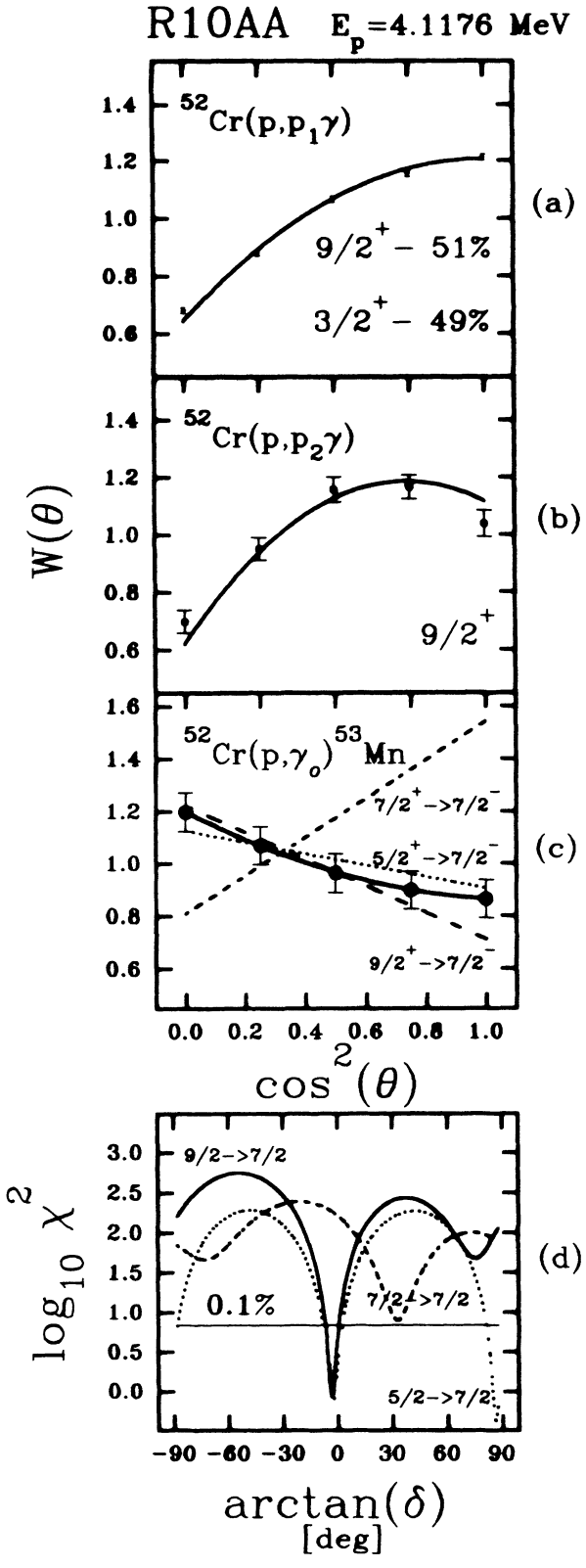

FIG. 6. The angular distributions measured at resonance R10AA and their analyses for the (a) $^{52}Cr(p,p_1\gamma)$, (b) $^{52}Cr(p,p_2\gamma)$ reactions and the (c) $^{52}Cr(p,\gamma_0)^{53}Mn$ reaction and (d) its χ^2 analysis. Details as in Fig. 5.

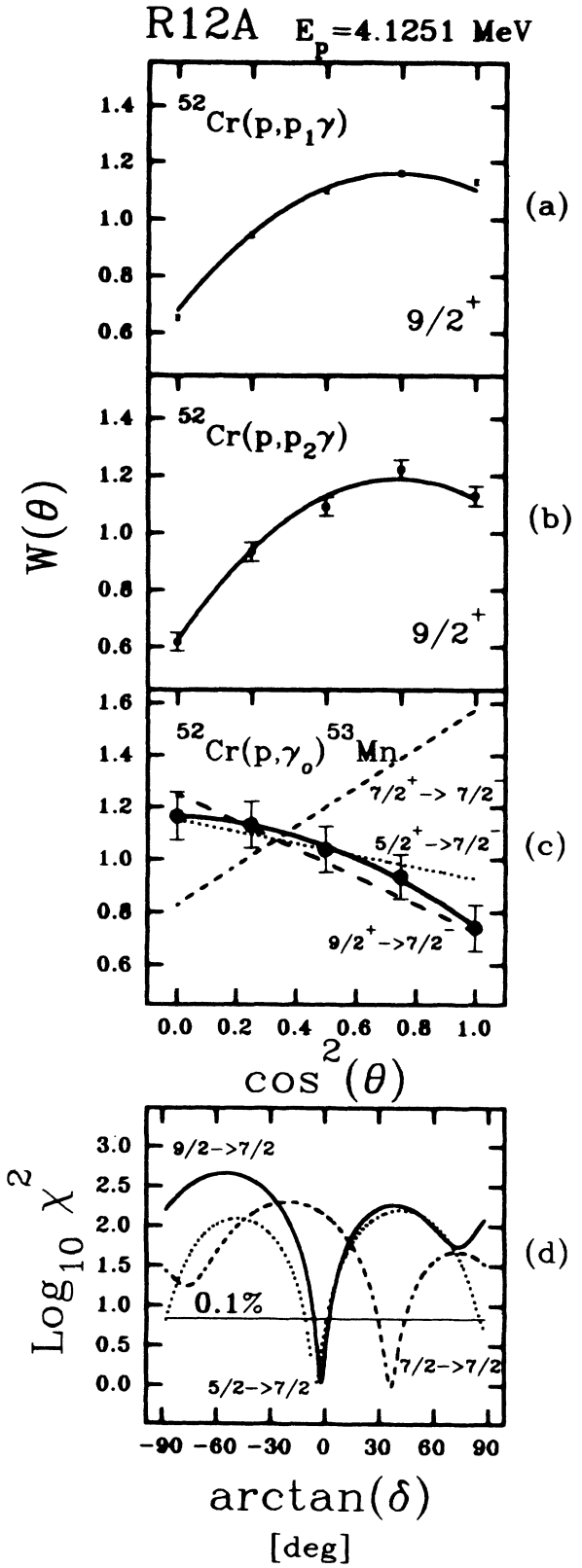

FIG. 7. The angular distributions measured at resonance R12A and their analyses for the (a) $^{52}Cr(p,p_1\gamma)$, (b) $^{52}Cr(p,p_2\gamma)$ reactions and the (c) $^{52}Cr(p,\gamma_0)^{53}Mn$ reaction and (d) its χ^2 analysis. Details as in Fig. 5.

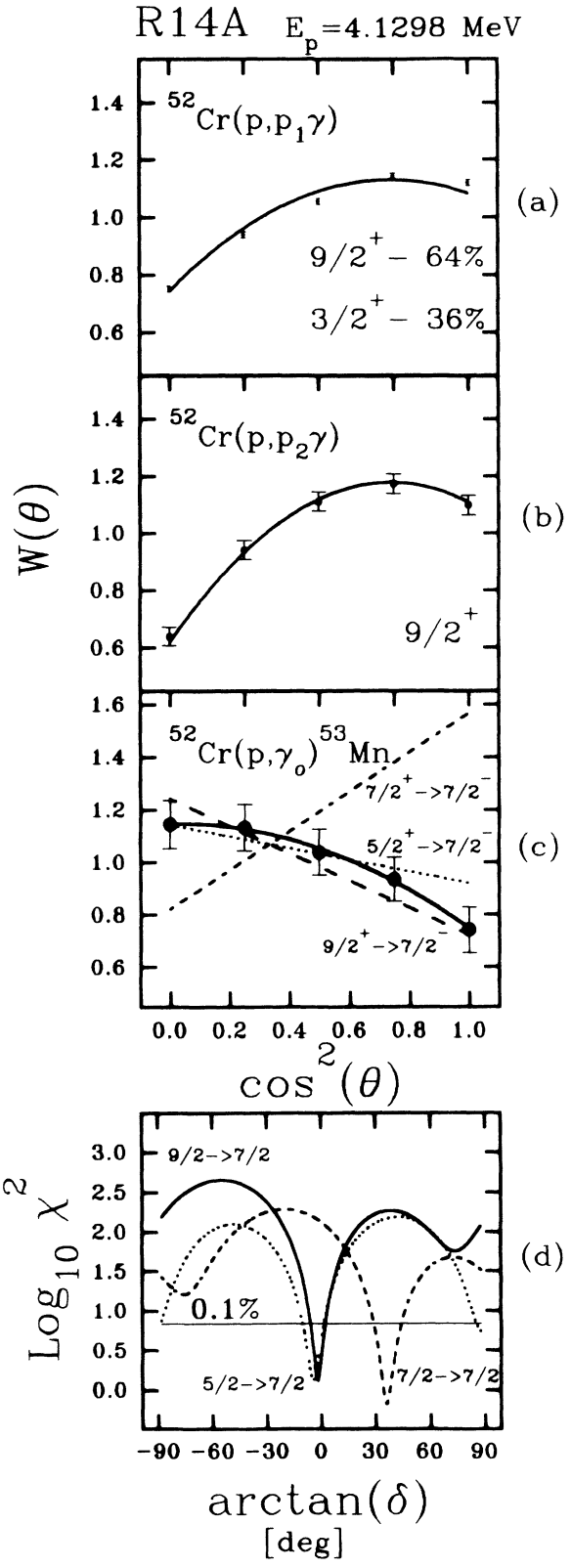

FIG. 8. The angular distributions measured at resonance R14A and their analyses for the (a) ^{52}Cr$(p,p_1\gamma)$, (b) ^{52}Cr$(p,p_2\gamma)$ reaction and the (c) ^{52}Cr$(p,\gamma_0)^{53}$Mn reaction and (d) its χ^2 analysis. Details as in Fig. 5.

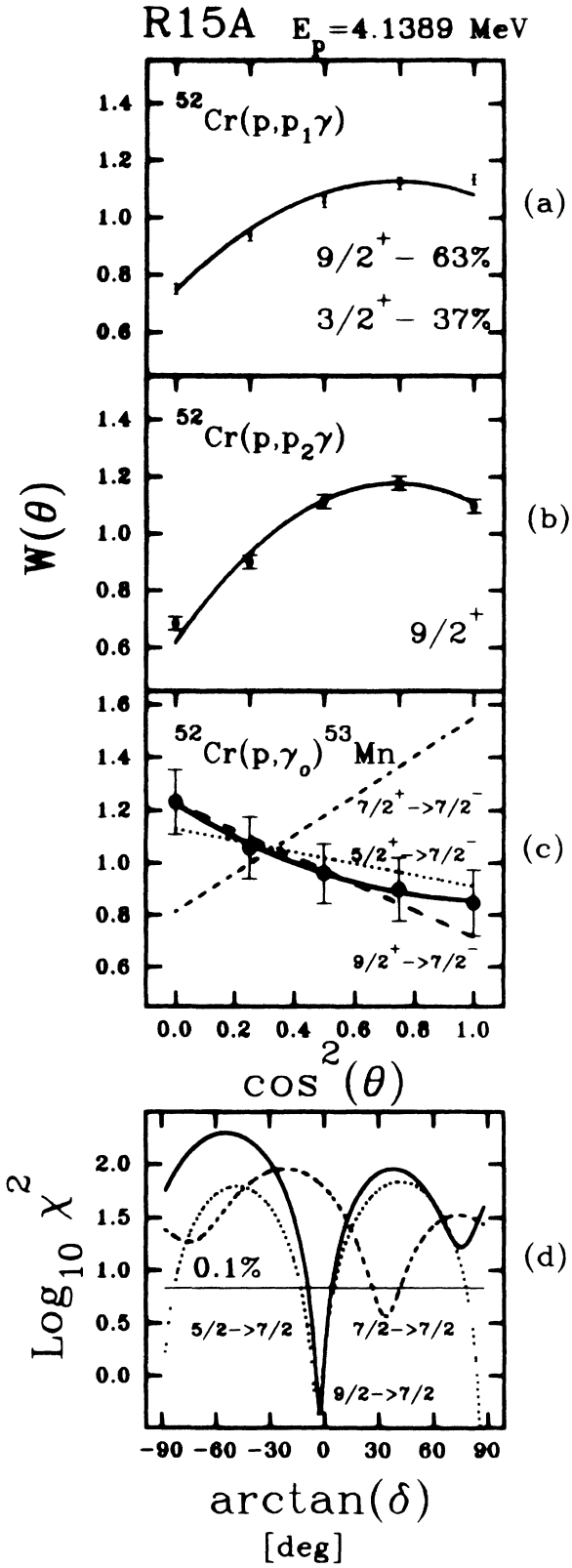

FIG. 9. The angular distributions measured at resonance R15A and their analyses for the (a) ^{52}Cr$(p,p_1\gamma)$, (b) ^{52}Cr$(p,p_2\gamma)$ reactions and the (c) ^{52}Cr$(p,\gamma_0)^{53}$Mn reaction and (d) its χ^2 analysis. Details as in Fig. 5.

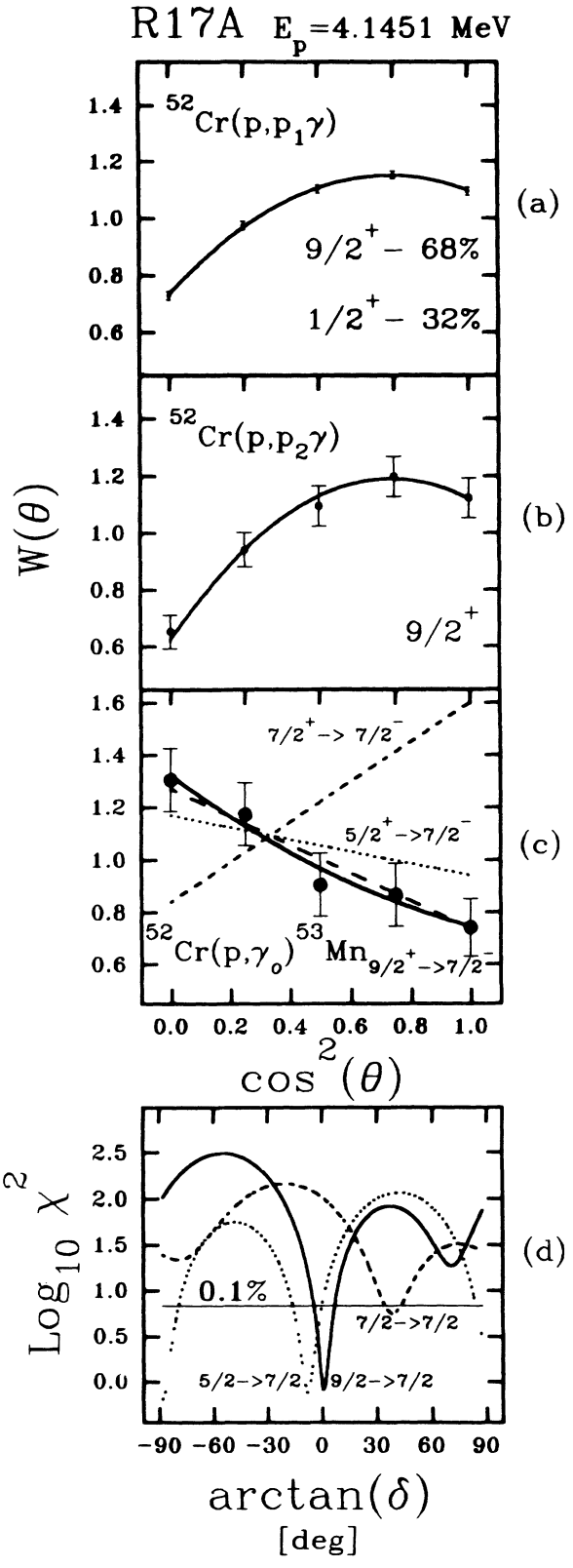

FIG. 10. The angular distributions measured at resonance R17A and their analyses for the (a) ^{52}Cr($p,p_1\gamma$), (b) ^{52}Cr($p,p_2\gamma$) reactions and the (c) ^{52}Cr(p,γ_0)^{53}Mn reaction and (d) its χ^2 analysis. Details as in Fig. 5.

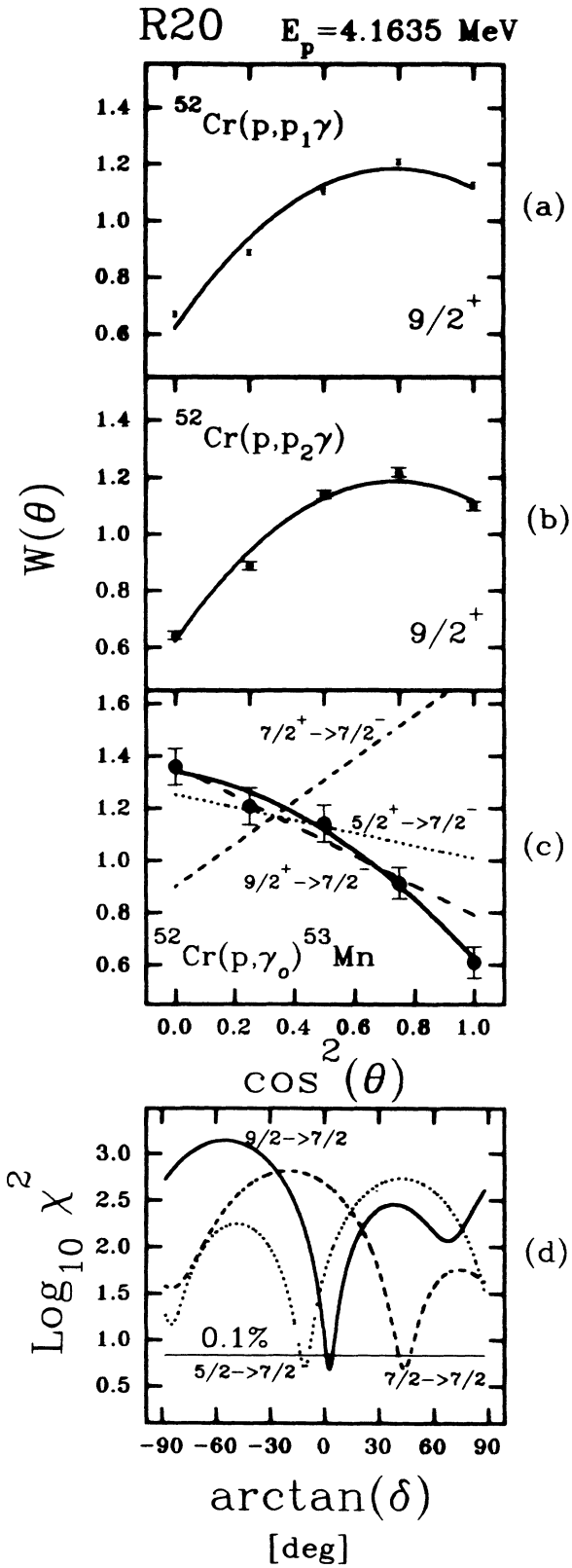

FIG. 11. The angular distributions measured at resonance R20 and their analyses for the (a) ^{52}Cr($p,p_1\gamma$), (b) ^{52}Cr($p,p_2\gamma$) reactions and the (c)^{52}Cr(p,γ_0)^{53}Mn reaction and (d) its χ^2 analysis. Details as in Fig. 5.

of the $1g_{9/2}$ IAR. The γ decay seems to be dominated by the $E1$ isovector ground-state transition. In the decay of some stronger resonances the population of the $E_x = 1.441$ MeV, $J^\pi = 11/2^-$ state plays an important role. Most of the fragments decayed to the $E_x = 2.573$ MeV, $J^\pi = 7/2^-$ state relatively strongly. The expected analog-to-antianalog $M1$ isovector transition, however, could not be identified from our γ-ray spectra, probably

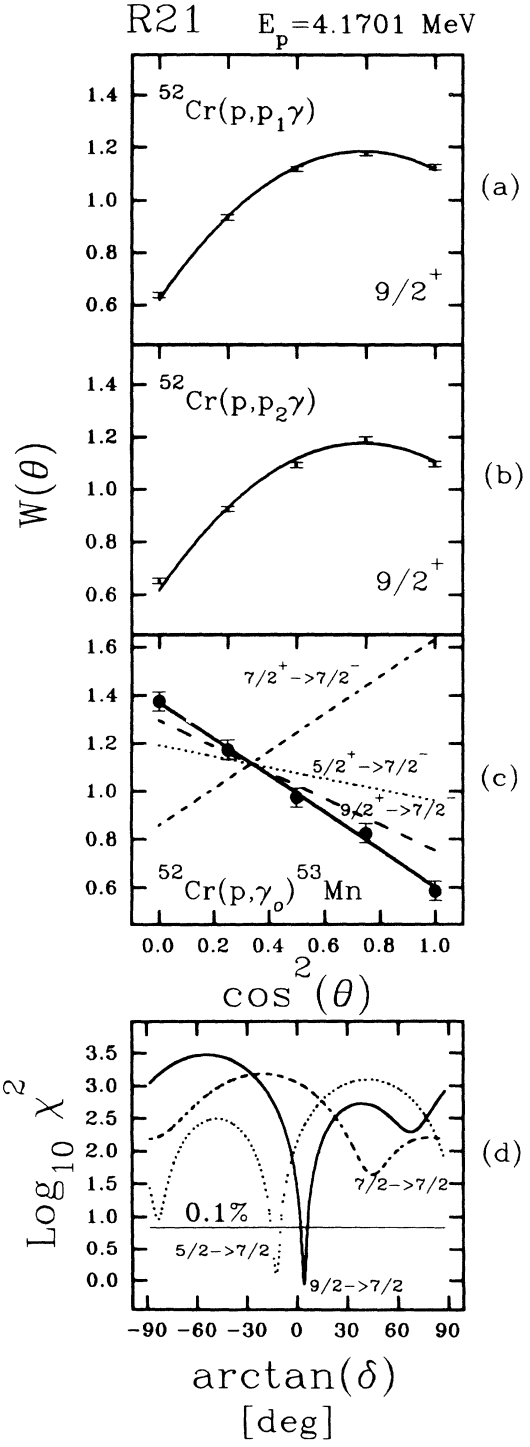

FIG. 12. The angular distributions measurd at resonance R21 and their analysis for the (a) ^{52}Cr$(p,p_1\gamma)$, (b) ^{52}Cr$(p,p_2\gamma)$ reaction and the (c) ^{52}Cr$(p,\gamma_0)^{53}$Mn reaction and (d) its χ^2 analysis. Details as in Fig. 5.

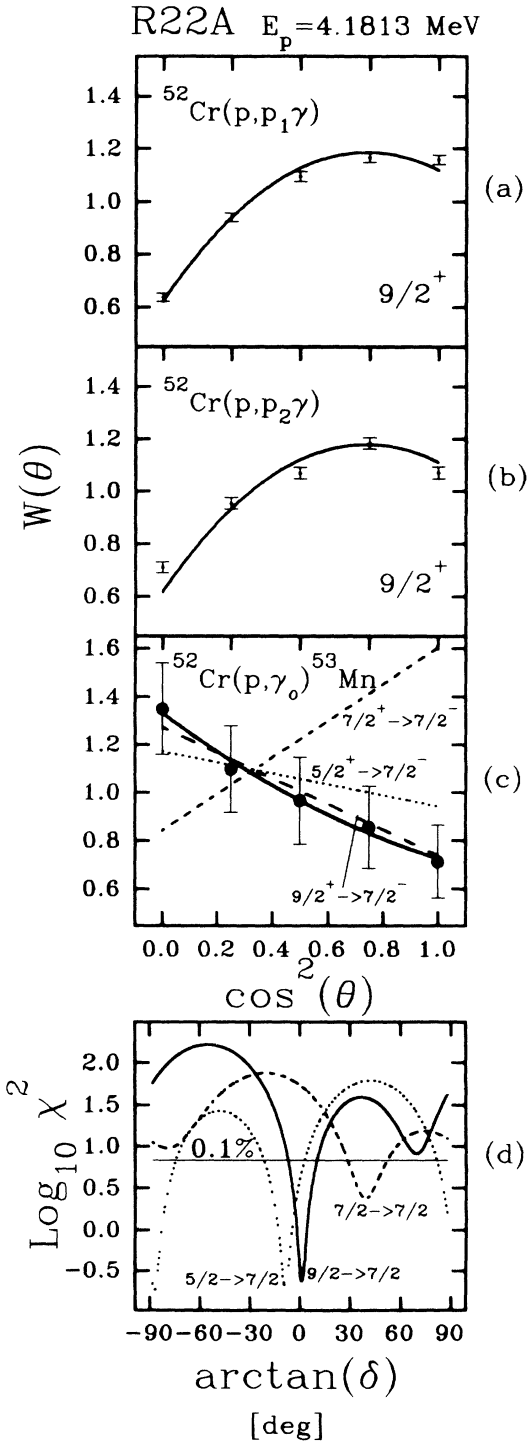

FIG. 13. The angular distributions measured at resonance R22A and their analyses for the (a) ^{52}Cr$(p,p_1\gamma)$, (b) ^{52}Cr$(p,p_2\gamma)$ reactions and the (c) ^{52}Cr$(p,\gamma_0)^{53}$Mn reaction and (d) its χ^2 analysis. Details as in Fig. 5.

due to the fact that the antianalog state lies very close to the particle emission threshold.

E. The partial strengths of the resonance fragments in different channels

From the analysis of the γ spectra measured on each $1g_{9/2}$ resonance fragment the $\Gamma_{p_0}\Gamma_i/\Gamma$ yields were derived, where Γ_{p_0} is the elastic proton partial width, Γ_i stands for the partial width [$i = p_1, p_2$, and $(\gamma_j, j = 0, 1, 2, ...)$ i.e., the observed first and second inelastic, and different γ decay channels], while $\Gamma = \Gamma_{p_0} + \Gamma_{p_1} + \Gamma_{p_2} + \Sigma_j \Gamma\gamma_j$ is the total width of the resonance fragment. In the present case the Γ_{p_0} and Γ_{p_1} partial widths were already available from the R-matrix analysis of the independent proton scattering experiment, thus the Γ_i partial widths for other channels could be determined directly from the measured yields. The availability of the Γ_{p_1} partial widths from two independent sources gave an excellent possibility for double-checking our data. The results are given in Table II. The uncertainties of the partial widths are estimated to be about 2–15 %.

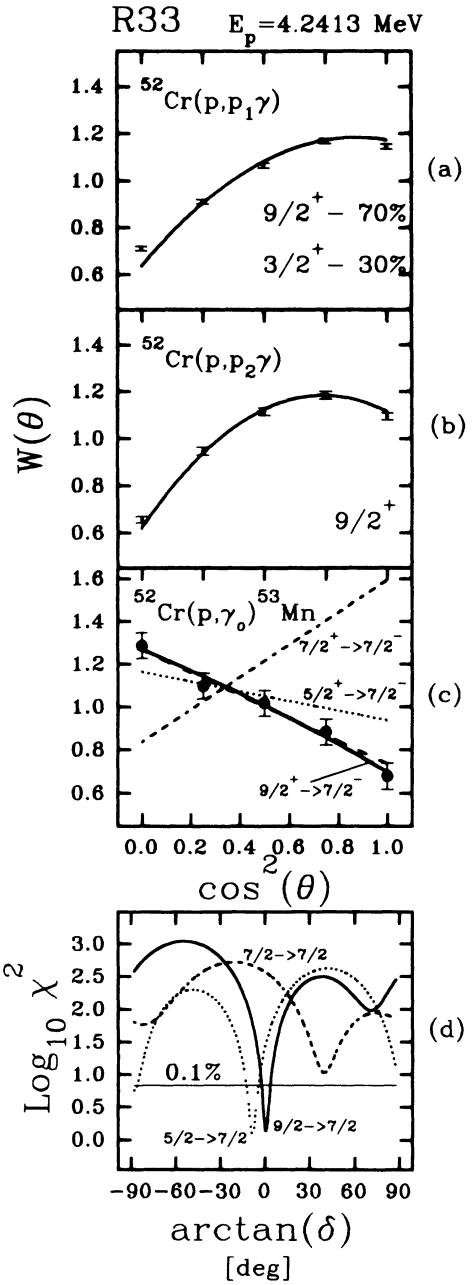

FIG. 14. The angular distributions measured at resonance R33 and their analyses for the (a) ^{52}Cr$(p, p_1\gamma)$, (b) ^{52}Cr$(p, p_2\gamma)$ reactions and the (c) ^{52}Cr$(p, \gamma_0)^{53}$Mn reaction and (d) its χ^2 analysis. Details as in Fig. 5.

F. Channel-channel correlations

In the study of the IAR fragmentation as a multichannel phenomena, one is concerned about the statistical significance of the appearance of the analog state in different channels. As it is to be seen from Table II, besides the elastic scattering, the inelastic scattering to both the first and the second excited states of the target nucleus are strongly enhanced by the $1g_{9/2}$ analog state. In order to establish the independence (or the lack of independence i.e., the correlation) of the two sets of partial widths, the standard linear correlation coefficient

$$r(x,y) = \frac{\sum_i (x_j - \bar{x})(y_i - \bar{y})}{\left[\sum_i (x_i - \bar{x})^2\right]^{1/2}\left[\sum_i (y_i - \bar{y})^2\right]^{1/2}} \quad (1)$$

was used, where $\{x_i\}$ and $\{y_i\}$ represent the two sets of partial widths, and $\bar{x}$ and $\bar{y}$ stand for the average of the partial widths in the two channels. In order to test the hypothesis that the widths are independent, one determines the probability α that a value of r as large as or larger than the observed r occurs for a random sample of widths. If α is small, the hypothesis of independence is rejected at significance level α, or the widths are correlated at confidence level of $1-\alpha$. The alternative physical hypothesis is that the analog state is a common doorway for the two channels, and thus there is a large correlation between the sets of widths in the two channels. Testing one hypothesis against an alternative hypothesis was considered in depth by Kendall [17]. Two different approaches are employed to evaluate confidence levels. One method is to assume a parent distribution for one set of widths, and then generate the distribution of r using Monte Carlo techniques. The other method is to apply the "distribution-free" test of statistical independence introduced by Baudinet-Robinet [18]. For testing our data this latter method was used, being a much simpler test for independence than the Monte Carlo test in the case of two sets of widths [19]. The channel-channel correlation results for the elastic, the first and second inelastic, and seven (p, γ) channels are given in Table III.

G. Spectroscopic factors

By definition, the spectroscopic factor is the ratio of the reduced width of the state to that of a single-particle state of the same spin-parity and at the same energy. The S_n neutron spectroscopic factor is obtained from a (d,p) study, in which, if stripping dominates, i.e., the parent state can be well described as a single neutron on a certain orbit coupled to the ground state of the target nucleus, S_n is the ratio of the observed cross section to that calculated for a single-particle state. Similarly one can evaluate the S_p proton spectroscopic factor for an unbound resonance by the ratio of the observed proton width to that of a single-particle resonance at the same energy. While the S_n is known from the (d,p) study and the related S_p can be evaluated and compared to it, there is no information available about the contributions originating from parent state configurations when the single

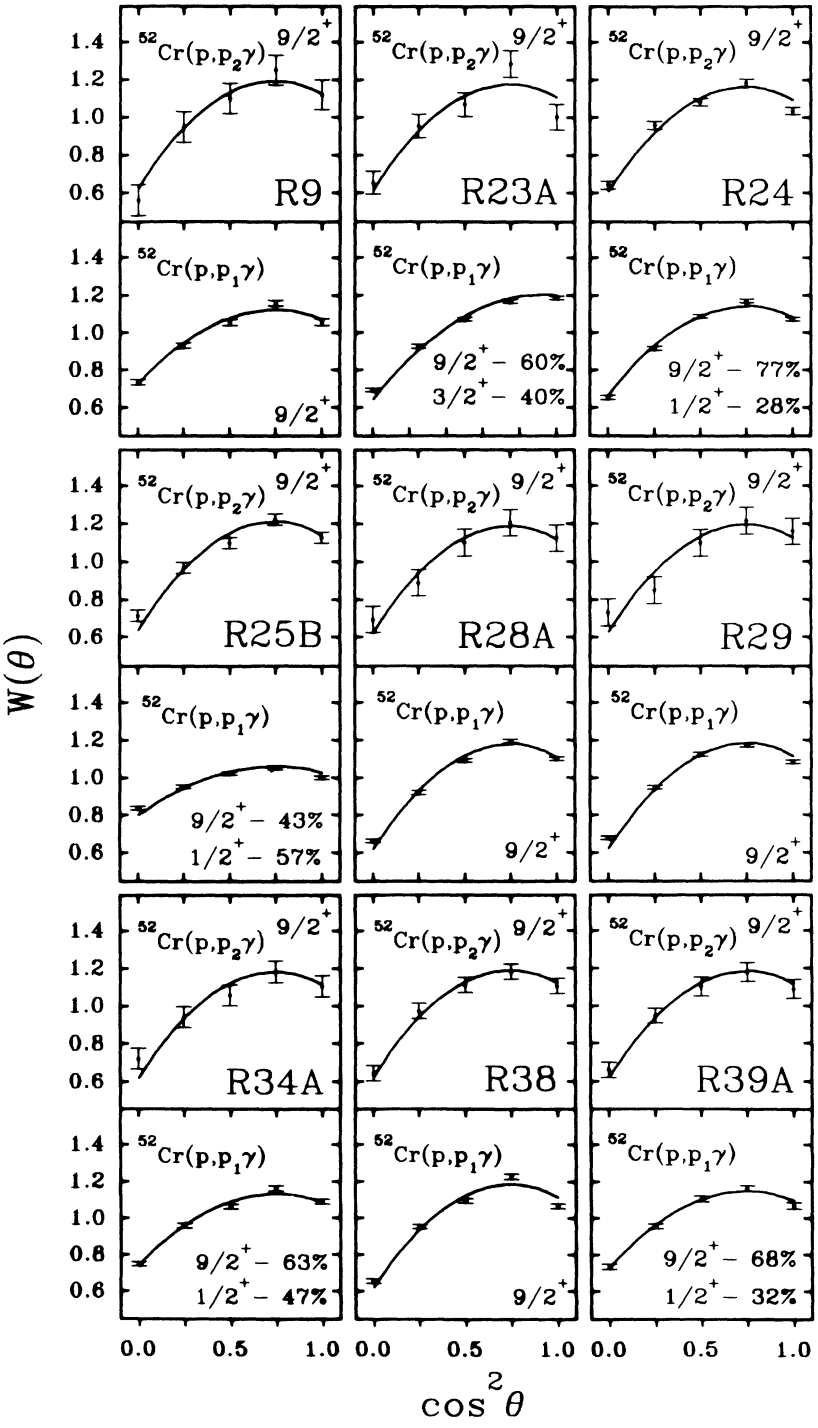

FIG. 15. The $^{52}Cr(p,p_1\gamma)$ and $^{52}Cr(p,p_2\gamma)$ angular distributions and their analyses for resonances R9-R39A.

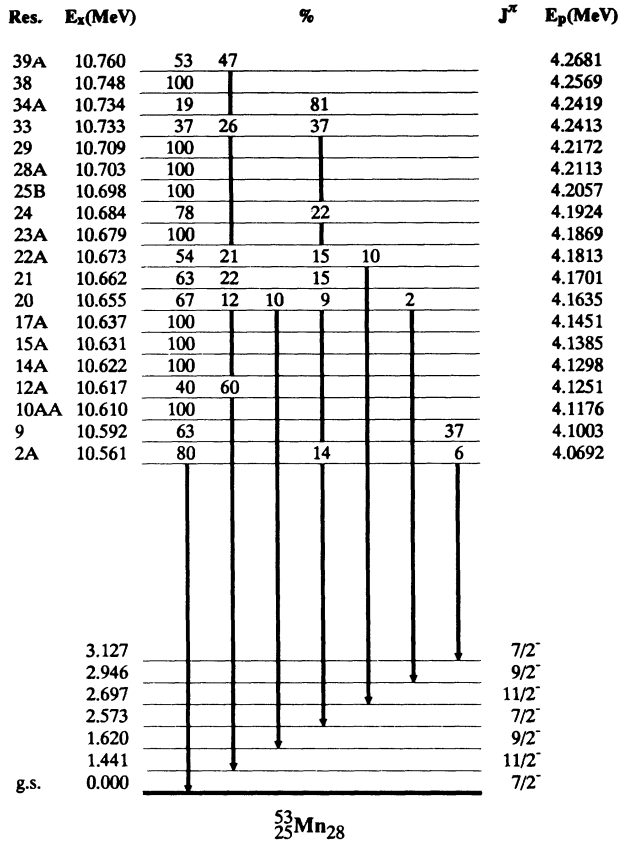

FIG. 16. The γ branchings for the fragments of the $1g_{9/2}$ IAR in ^{53}Mn. The errors are estimated to be about 2%.

neutron is coupled to different core-excited states of the target nucleus.

The appearance of the $\frac{9}{2}^+$ resonance in the inelastic channels strongly suggests that the wave function of this analog state and that of its fragments contain non-negligible terms corresponding to configurations when the proton on a single-particle orbit is coupled to the first and second core-excited states of the target nucleus. The inelastic spectroscopic factor is the ratio of the reduced partial width of the $\frac{9}{2}^+$ state in a given inelastic channel to that of a single-particle state of the same spin parity and at the same energy. Its value gives the measure of how important this inelastic term is in the formation and decay of this IAR.

The elastic and inelastic spectroscopic factors for the $\frac{9}{2}^+$ resonance were derived from the sums of the elastic and inelastic partial widths using the formula

$$S_{p_i} = (2T_0 + 1)\frac{\sum \Gamma_p^i}{\Gamma_{sp}^i}, \tag{2}$$

where i refers to the elastic ($i = 0$) and to the first and second inelastic ($i = 1, 2$) spectroscopic factor. T_0 is the isospin of the target nucleus, $\sum \Gamma_p^i$ stands for the sum of the partial widths, and Γ_{sp}^i is the single-particle width calculated with program HANS [20]. The results are presented in Table IV.

IV. THE FINE STRUCTURE ANALYSES

To obtain quantitative results describing the behavior of the distribution of the partial widths of the fragments of the $1g_{9/2}$ IAR in ^{53}Mn, fine structure analyses

TABLE II. Partial widths of the fragments of the $1g_{9/2}$ IAR identified in the ^{52}Cr(p,p_0), ^{52}Cr(p,p_1), ^{52}Cr$(p,p_1\gamma)$, ^{52}Cr$(p,p_2\gamma)$, and ^{52}Cr$(p,\gamma_0)^{53}$Mn reactions.

Fragment's		(p,p_0)		(p,p_1)		(p,p_2)					(p,γ)			
No.	E_p^{lab} (MeV)	Γ_{p_0} (eV)	$\gamma_{p_0}^2$ (keV)	Γ_{p_1} (eV)	$\gamma_{p_1}^2$ (keV)	Γ_{p_2} (eV)	$\gamma_{p_2}^2$ (eV)	Γ_{γ_0} (eV)	$\Gamma_{\gamma_{1441}}$ (eV)	$\Gamma_{\gamma_{1620}}$ (eV)	$\Gamma_{\gamma_{2573}}$ (eV)	$\Gamma_{\gamma_{2697}}$ (eV)	$\Gamma_{\gamma_{2946}}$ (eV)	$\Gamma_{\gamma_{3127}}$ (eV)
2A	4.0692	15	3.13	2	0.13	0.10	21	0.21			0.03			0.01
9	4.1003	15	2.96	2	0.12	0.03	5	0.06						0.03
10AA	4.1176	30	5.74	2	0.12	0.08	12	0.05						
12A	4.1251	7	1.32	3	0.17	0.25	37	0.07	0.09					
14A	4.1298	14	2.62	7	0.39	0.44	64	0.10						
15A	4.1389	20	3.69	1	0.06	0.07	9	0.01						
17A	4.1451	2	0.37	1	0.05	0.06	7	0.04						
20	4.1635	48	8.47	20	1.03	2.49	300	1.00	0.15	0.12	0.11		0.03	
21	4.1701	75	13.09	60	3.05	2.71	315	0.31	0.10		0.07			
22A	4.1813	10	1.71	6	0.30	0.55	61	0.07	0.02		0.02	0.02		
23A	4.1869	4	0.68	12	0.58	0.29	30	0.11						
24	4.1924	2	0.34	10	0.48	1.25	126	0.07			0.03			
25B	4.2057	5	0.80	3	0.14	0.46	45	0.06						
28A	4.2113	3	0.49	2	0.09	0.02	2	0.04						
29	4.2172	5	0.80	6	0.27	0.06	6	0.12						
33	4.2413	10	1.54	14	0.60	2.90	236	0.64	0.44		0.52			
34A	4.2419	5	0.77	2	0.09	0.22	17	0.15			0.51			
38	4.2569	4	0.60	8	0.39	1.25	93	0.05						
39A	4.2681	3	0.44	3	0.12	0.24	17	0.048	0.042					

TABLE III. Channel-channel correlations for the $1g_{9/2}$ analog state in ^{53}Mn. The confidence levels for the set of ten elastic widths correlated with ten random widths are: 80% (0.25), 90% (0.51), 95% (0.67), and 99% (0.88).

J^{π}_{final}	Channel	p,p_0	p,p_1	p,p_2	p,γ_0	p,γ_{1441}	p,γ_{1620}	p,γ_{2573}	p,γ_{2697}	p,γ_{2946}	p,γ_{3127}
0^+	p,p_0	1	0.83	0.71	0.50	0.22	0.44	0.02	−0.06	0.44	−0.01
2^+	p,p_1		1	0.81	0.43	0.34	0.21	0.12	−0.05	0.21	−0.16
4^+	p,p_2			1	0.80	0.65	0.55	0.35	−0.03	0.55	−0.21
$7/2^-$	p,γ_0				1	0.71	0.81	0.47	−0.10	0.81	−0.13
$11/2^-$	p,γ_{1441}					1	0.24	0.66	−0.06	0.24	−0.14
$9/2^-$	p,γ_{1620}						1	0.06	−0.06	0.99	−0.08
$7/2^-$	p,γ_{2573}							1	−0.07	0.06	−0.12
$11/2^-$	p,γ_{2697}								1	−0.06	−0.08
$9/2^-$	p,γ_{2946}									1	−0.08
$7/2^-$	p,γ_{3127}										1

were carried out independently in all channels. To be free of the effect of the Coulomb barrier for the particle channels, the γ^2_λ reduced partial widths were used. For the ground-state capture channel the Γ_{γ_0} partial widths were used. For the fine structure analysis the method of MaDonald–Mekjian–Kerman–De Toledo Piza (MMKP) [21,22] was used. The Lorentz-weighted average of the partial widths (i.e., the experimental strength function) is

$$S(E;I) \equiv \langle \gamma^2_\lambda / D_\lambda \rangle = \frac{I}{\pi} \sum_\lambda \frac{\gamma^2_\lambda}{(E-E_\lambda)^2 + I^2}, \qquad (3)$$

where D_λ is the mean level spacing, and I is the width of the Lorentz weight of averaging. This was least-squares fitted by the parametric form of the analog doorway strength function [23]

$$S^D(E;I) = S_0 + \frac{1}{\pi}\frac{\gamma^2_A}{\cos^2\varphi}\frac{(I+\Gamma_s/2)\cos 2\varphi - (E-\hat{E}_A)\sin 2\varphi}{(E-\hat{E}_A)+(I+\Gamma_s/2)^2}, \qquad (4)$$

where S_0 is the background strength function, γ^2_A is the total width of the analog state, Γ_s is the spreading width, the parameter that measures the strength of the spreading and depends directly on the mean value of the doorway-hallway coupling matrix elements [23]. This coupling of the doorway state to more complicated hallway states makes the doorway state share its strength among the hallway states. The parameter $\hat{E}_A = E_A + \Delta_A$ gives the energy of the analog state containing the analog shift Δ_A arising also from the doorway-hallway coupling. Usually Δ_A is considered to be negligible. The parameter φ describes the asymmetry of the strengths around the centroid of the analog state.

For an MMKP-type strength function analysis one has to be very careful regarding the following parameters having influence on the fitting procedure: (i) the energy region of the fit; (ii) the number of points at which the experimental strength function is calculated from the experimental partial widths using Eq. (3); (iii) the value of I, the Lorentz weight of averaging; and (iv) the error propagation in the fine structure analysis of the MMKP type.

The energy region of the fit around the assumed centroid of the analog state is chosen in order to avoid meaningless edge effects of distant resonances. On the other hand, it should be large enough to contain the most important part of the experimental strength function even for the case of larger I averaging intervals.

The experimental strength function is smooth continuous curve calculated at several points. In principle the number of points for the fit has effect on the goodness of the fit because the parameters of the parametric theoretical MMKP strength function [Eq. (4)] are varied until the minimum of the χ^2 is reached.

In practice the best fit was found when $\chi^2/N \approx 1$ was achieved. The results of the fit do not depend on the number of points, the only condition being $\frac{1}{2}I > \langle D_\lambda \rangle$, the mean level spacing of the fragments. This latter relation gives a lower limit for I. To determine this lower limit the method of Dubois [24] was used. We can assume that the $9/2^+$ spin hallway states are distributed nearly at random, i.e., the probability of a level occurring in an interval ΔS at a distance S from a particular level

TABLE IV. Elastic and inelastic spectroscopic factors for the $1g_{9/2}$ IAR in ^{53}Mn. For details on differences in the values given by the different methods used, see Ref. [20].

E_x^{parent}		S_{pp}			S_{pp_1}			S_{pp_2}		
(MeV)	S_n[a]	(TAR)	(ZDH)	(MM)	(TAR)	(ZDH)	(MM)	(TAR)	(ZDH)	(MM)
3.715	0.57	0.53	0.55	0.54	0.12	0.11	0.11	0.03	0.02	0.02

[a]Reference [14].

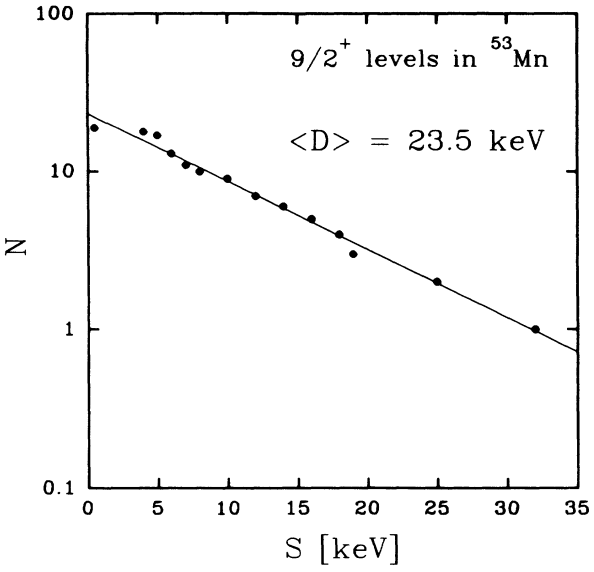

FIG. 17. Number of spacings N larger than S keV for the $9/2^+$ fragments in ^{53}Mn. The dots represents the experimental data, and the line is a linear regression curve to the data.

does not depend on S. We can then write the number of levels with spacings larger than S as

$$N = N_0 e^{-S/\langle D_\lambda \rangle},$$

where $\langle D_\lambda \rangle$ is the average spacing. Figure 17 shows that the experimental data follow the assumed distribution well. The lack of small spacings is mostly due to the finite energy resolution achieved. The result $\langle D_\lambda \rangle = 23.5$ keV, sets the lower limit for the proper Lorentz-weight of averaging being $I > 47$ keV.

The last crucial point is the equation of the error propagation in the fine structure analysis of MMKP type, i.e., how the errors of the original partial widths are influencing the uncertainties of the fine structure parameters. The statistical signifance of the parameters obtained in an MMKP-type fine structure analysis was throughout tested theoretically and statistically [26] and it was proved, that if the Lorentz averaging width I is chosen properly, the accuracy of the spreading width can be better than 10% even for the so called "weak coupling" case. On the other hand, the error propagation in a fine structure analysis of MMKP-type was considered analytically, and in a previous work [11] an *upper estimate* for the uncertainties [Eq. (A5) of Ref. [11]] of the smooth experimental strength function originating from the uncertainties of the experimental partial widths was derived. It was shown that extremely large initial errors have a different effect on the uncertainties of the resulting fine structure parameters. The resulting uncertainties of parameters E_A and γ_A^2 are almost insensitive for the increased size of the initial errors. The uncertainties of the spreading width Γ_s are only moderately influenced, while the uncertainties of S_o and the asymmetry parameter φ are considerably increased by extremely large initial errors. These above results strongly suggested that the analyses performed with these *upper estimated* errors supply reliable sets of parameters characterizing the fragmentation.

The fitting procedures for the different channels were carried out independently, and repeated with increasing averaging widths I until the resulting fine structure parameters became *independent* of I itself. This usually occurred, as mentioned earlier, at $\chi^2/N \approx 1$. Some details of the fitting procedures carried out in different channels are illustrated in Figs. 18–25. The averaging width I was increased from $I = 5$ keV to 200 keV in steps of 5 keV. The resulting fine structure parameters served as input parameters for the next fit. Figure 18

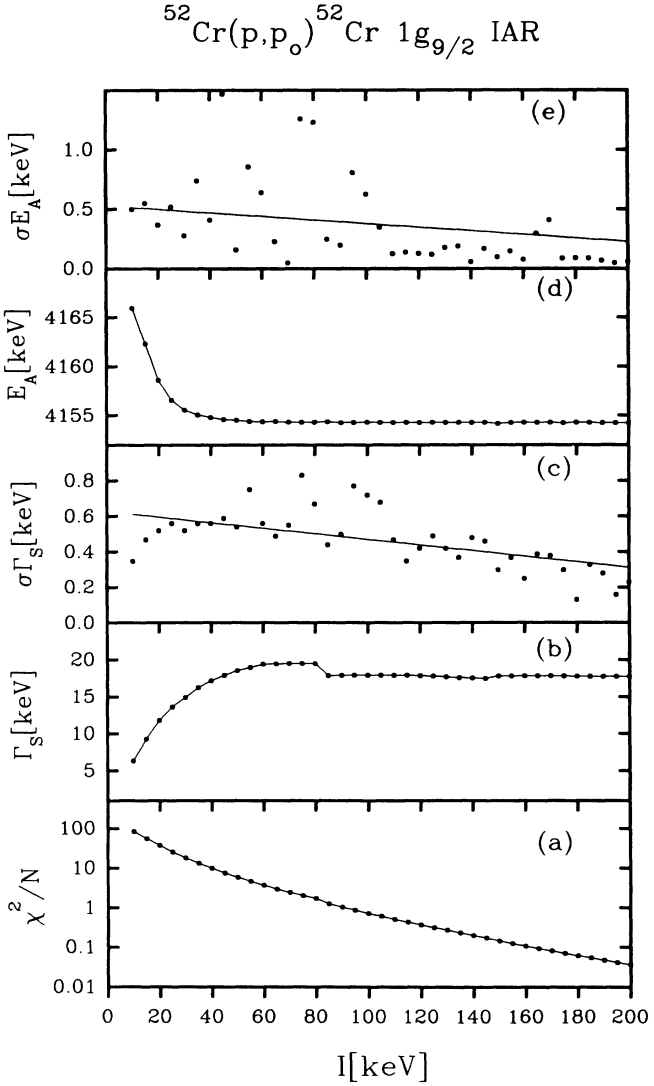

FIG. 18. The dependence of the most important fine structure parameters, i.e., the spreading width Γ_S and the centroid energy of the IAR E_A and their resulting uncertainties, together with the χ^2/N (N=400) on I for the ^{52}Cr(p, p_0) reaction channel.

shows the dependence of the most important parameters i.e., the spreading width Γ_S and the centroid energy of the IAR E_A and their resulting uncertainties, together with the χ^2/N (N=400 in the present case) on I for the ^{52}Cr(p,p_0) reaction. It is seen how the parameters are becoming independent from I after $t\chi^2/N$ reaches ≈ 1. Figures 18(c) and 18(e) show the behavior of the uncertainties $\sigma\Gamma_S$ and σE_A, respectively. The values are well scattered along the regression lines and are decreasing with increasing I. Figure 19 shows the distribution of the elastic reduced partial widths (a) together with fits of the MMKP-type theoretical strength functions (lines) to the experimental ones (dots) for I = 10 keV (b), 50 keV (c), 100 keV (d), and 150 keV (e) Lorentz averaging intervals. Figures 20–25 give the same for the first and second inelastic, and for the (p,γ_0) channels. The fine structure parameters obtained for the four reaction channels are listed in Table V.

V. DISCUSSION AND CONCLUSIONS

The high sensitivity and selectivity of the (p,p_2) reaction for higher spin resonances, the use of simultaneous excitation function, angular distribution measurements, and their analyses in all open reaction channels enabled the identification and study even of the weaker fragments of the $1g_{9/2}$ resonance in ^{53}Mn.

The comparison of the identified $1g_{9/2}$ partial strengths with results from previous experiments [5–9] is rather difficult, since the differences in the applied energy resolutions make it impossible to find correspondence in the number and in the positions of the $1g_{9/2}$ IAR fragments. On the other hand, the only high resolution work, by Ozawa *et al.* [13], identified only one fragment.

Comparing our results with that of the work of Ozawa *et al.* [13] one can state the following. There are fairly

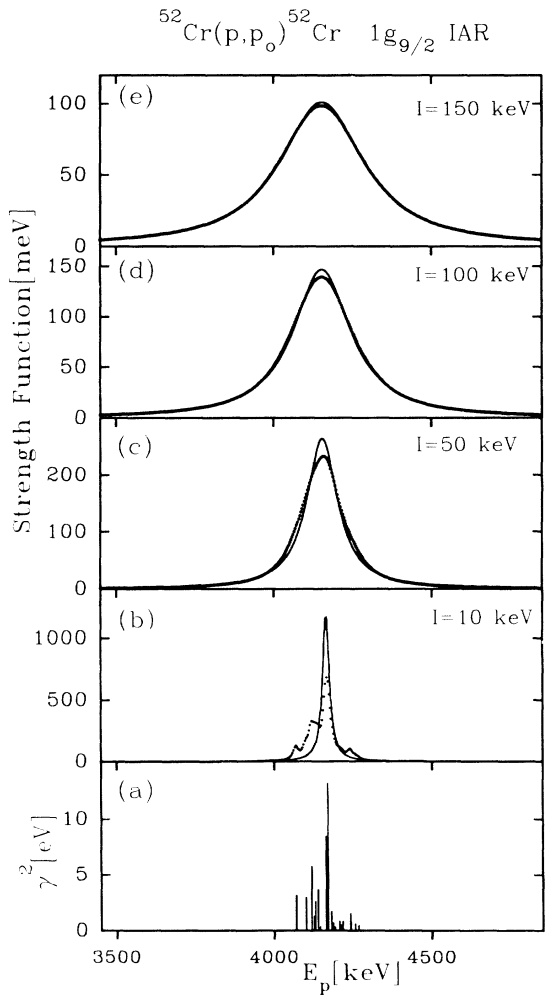

FIG. 19. The distribution of the elastic reduced partial widths (a) together with fits of the MMKP-type theoretical strength functions (lines) to the experimental ones (dots) for I = 10 keV (b), 50 keV (c), 100 keV (d), and 150 keV (e) Lorentz averaging intervals.

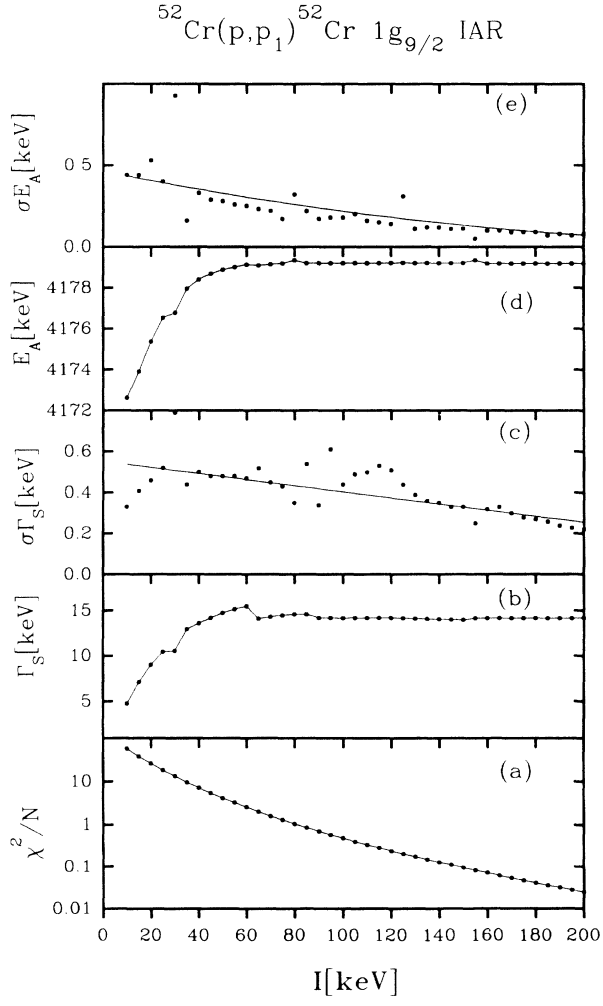

FIG. 20. The dependence of the most important fine structure parameters i.e., the spreading width Γ_S and the centroid energy of the IAR E_A and their resulting uncertainties, together with the χ^2/N (N=400) on I for the ^{52}Cr(p,p_1) reaction channel.

TABLE V. Fine structure parameters for the $1g_{9/2}$ IAR in ^{53}Mn for the ^{52}Cr(p,p_0), $^{52}(p,p_1)$, $^{52}(p,p_2)$, and ^{52}Cr$(p,\gamma_0)^{53}$Mn reaction channels.

E_x^{parent} (MeV)		(p,p_0)	(p,p_1)	(p,p_2)	(p,γ_0)
3.715(5)	E_A(MeV)	4.154(2)	4.179(1)	4.187(3)	4.182(1)
	S_o(keV)	−0.36(20)	−0.051(2)	−0.011(2)	−0.036(2)
	γ_A^2(keV)	49.319(2)	8.057(8)	1.392(6)	3.284(5)[a]
	Γ_s(keV)	18(1)	14(1)	18(1)	25(1)
	tanφ	0.005(6)	0.003(2)	−0.006(2)	0.001(2)
	I(keV)	90	80	90	110

[a]Γ_A [eV].

good agreements in the positions of some of the stronger $\frac{1}{2}^+$ resonances, but the partial and total widths are different for many cases, and about half of the weaker $\frac{1}{2}^+$ resonances were not reported by Ozawa *et al.* [13]. There are, however, other differences in the spin assignments for the $l = 1$ and $l = 2$ resonances, since many of the $l = 2$ resonances were assigned as $\frac{3}{2}^+$, while already the preliminary $(p,p_1\gamma)$ angular distributions [12] showed a clear $\frac{5}{2}$ character. The similar can be said about the $l = 1$ resonances, because many of them reported as $\frac{1}{2}^-$

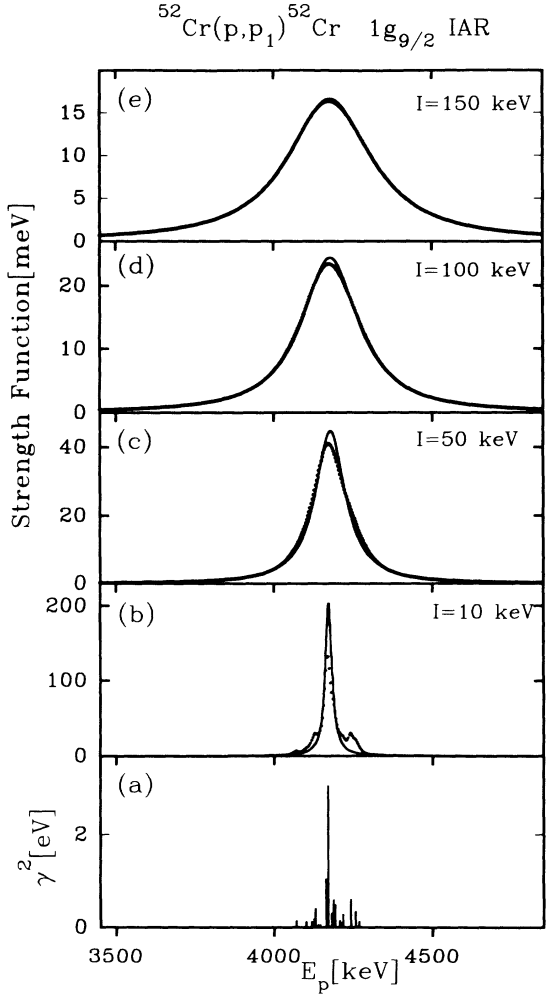

FIG. 21. The distribution of the first inelastic reduced partial widths (a) together with fits of the MMKP-type theoretical strength functions (lines) to the experimental ones (dots) for I=10 keV (b), 50 keV (c), 100 keV (d) and 150 keV (e) Lorentz averaging intervals.

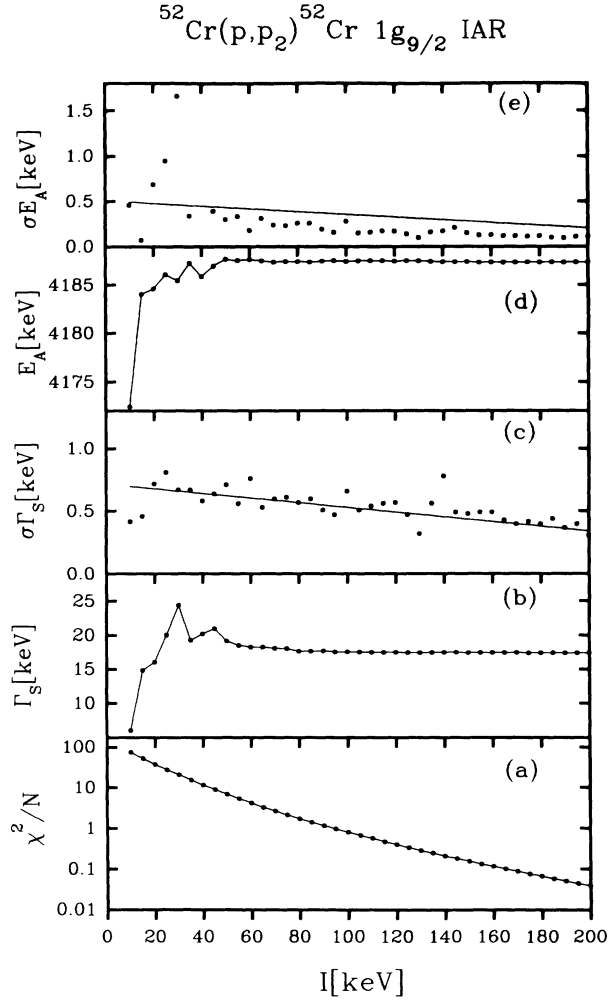

FIG. 22. The dependence of the most important fine structure parameters i.e., the spreading width Γ_S and the centroid energy of the IAR E_A and their resulting uncertainties, together with the χ^2/N (N=400) on I for the ^{52}Cr(p,p_2) reaction channel.

showed no isotropic $(p, p_1\gamma)$ angular distributions, but rather showed a clear $\frac{3}{2}$ character. The most important disagreements occur in the regions of the 19 identified $\frac{9}{2}^+$ resonances. Ozawa *et al.* [13] reported mainly $\frac{5}{2}^+$ resonances and achieved poor fits to the experimental data. Inclusion of the $\frac{9}{2}^+$ resonances greatly improved the quality of the fits at all angles, and especially in the inelastic channel.

Table III gives the derived channel-channel correlations for ten channels. The large correlations found give the evidence that the patial strengths in the inelastic, and some of the capture channels, considering the given confidence levels, are highly correlated with the elastic ones, and with each other too. This indicates that the analog state acts as a common doorway [25] for the decay channels studied.

As it can be seen from Table IV, the derived elastic spectroscopic factor agrees well with the spectroscopic factor of the parent state. It means that the majority of the parent single-particle strength was found. The first inelastic spectroscopic factor is fairly large and the second inelastic spectroscopic factor is also non-negligible. Comparing these inelastic spectroscopic factors with results from a previous work on the $^{50}Cr + p$ system [11] one can state, that their corresponding values are very close to each other. This gives the evidence that the wave function of the $1g_{9/2}$ parent state in ^{53}Cr, similarly to the ones in ^{51}Cr, contains non-negligible terms corresponding to configurations where the single-particle neutron is coupled to the first (2^+) and second (4^+) core-excited states of the ^{52}Cr target nucleus.

Table V gives the result of the fine structure analyses carried out in the four channels. Based on these results the following can be stated: (i) The fits were made independently, and the presumably channel-independent parameters, i.e., the spreading width Γ_S and the centroid energy of the IAR E_A in different channels show non-negligible differences. (ii) The position of the analog

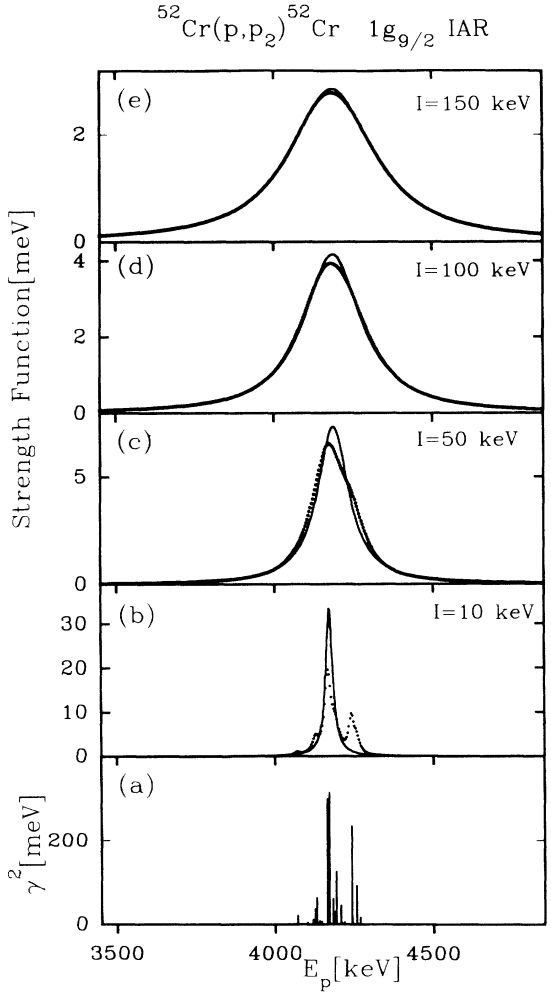

FIG. 23. The distribution of the second inelastic reduced partial widths (a) together with fits of the MMKP-type theoretical strength functions (lines) to the experimental ones (dots) for I=10 keV (b), 50 keV (c), 100 keV (d) and 150 keV (e) Lorentz averaging intervals.

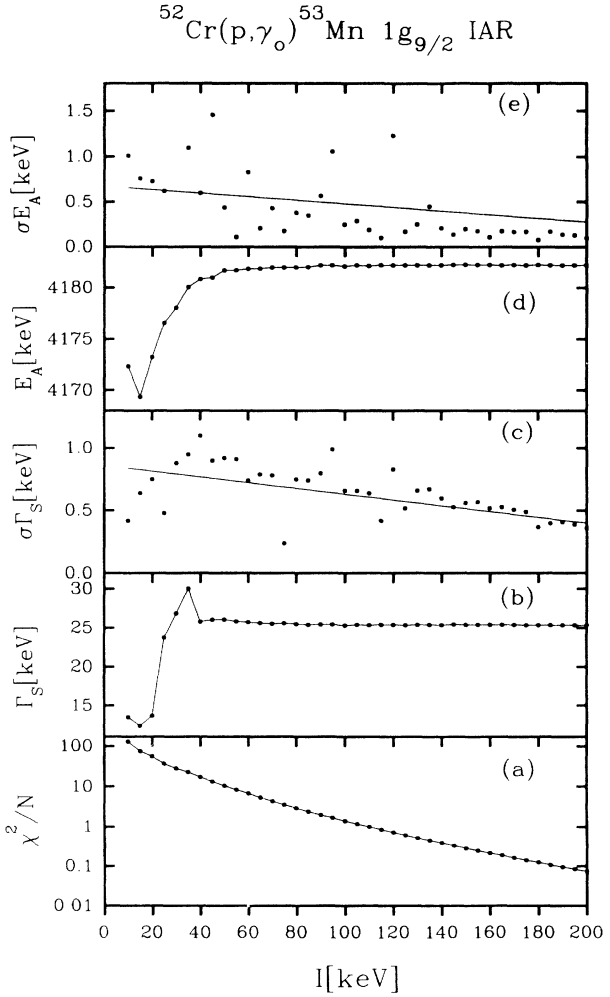

FIG. 24. The dependence of the most important fine structure parameters, i.e., the spreading width Γ_S and the centroid energy of the IAR E_A and their resulting uncertainties, together with the χ^2/N (N=400) on I for the $^{52}Cr(p, \gamma_0)^{53}Mn$ reaction channel.

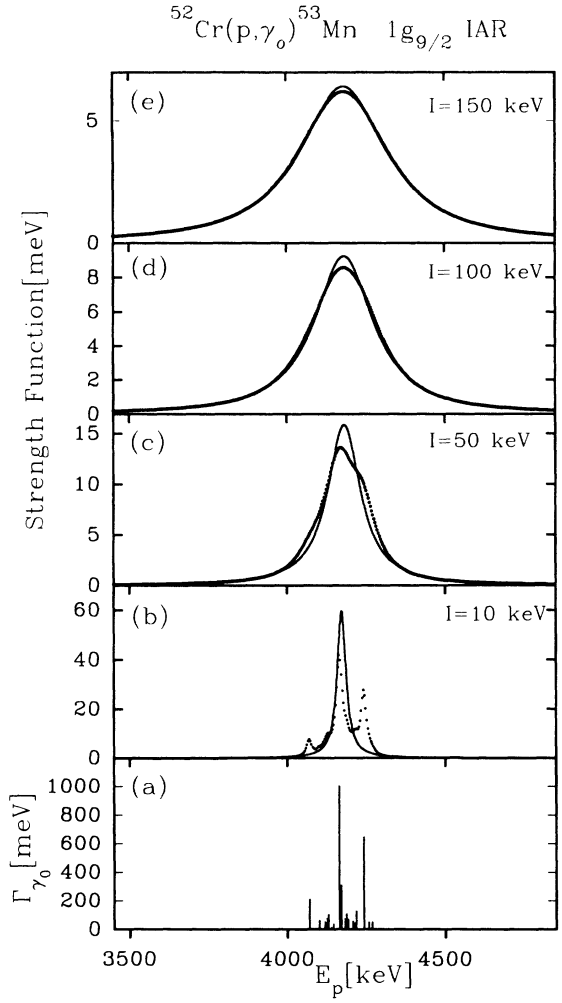

FIG. 25. The distribution of the (p,γ_0) partial widths (a) together with fits of the MMKP-type theoretical strength functions (lines) to the experimental ones (dots) for I=10 keV (b), 50 keV (c), 100 keV (d), and 150 keV (e) Lorentz averaging intervals.

state energy is about 28 keV lower in the (p,p_0) channel than in all other channels. (iii) The background strength functions are fairly weak in all channels. The small negative values suggest that some very weak fragments still remained unidentified by the present work. (iv) The total reduced widths are very well reproduced in all channels. (v) The spreading widths are the same in the (p,p_0) and (p,p_2) channels and are slightly larger than in the (p,p_1) channel. The spreading width in the (p,γ_0) channel, however, is about twice as large as the one in the (p,p_1) channel. Even if one is skeptical about the cited uncertainties, these differences are nonnegligible, and these cannot be explained with the available theories [18–20]. (vi) The asymmetry parameter φ is practically zero for all channels showing that there is no significant asymmetry for this $1g_{9/2}$ IAR.

TABLE VI. Comparison of the Coulomb displacement energies for the $1g_{9/2}$ IAR in ^{53}Mn.

Parent state E_x (MeV)	Present work ΔE_c (MeV)	Ref. [6] ΔE_c (MeV)
3.715(6)	8.379(15)	8.333(12)

When carrying out fine structure analysis of an analog state in different channels, based on available theories, one expects to obtain the same E_A, Γ_S, and tanφ fine structure parameters in all channels, at least within the uncertainties resulting from the fitting procedure, since these parameters are the properties of the analog state, not the channel of the observation. The other two parameters S_0 and γ_A^2, determined by the partial widths in the actual channel, are naturally channel depdendent.

To solve these disagreements further theoretical work involving the configurations where the parent state is considered to be built up from more than one configuration (containing the one neutron coupled to not only the 0^+, but the 2^+ and 4^+ core excited states) would be desirable.

From the position of the $1g_{9/2}$ analog state in the (p,p_0) channel the experimental Coulomb displacement energy was calculated. The comparison with results from Ref. [6] is given in Table VI. Our value is about 46 keV higher than the one given by Galès *et al.* [6]. This may originate from the fact that some higher-lying stronger fragments were not seen in their experiment.

ACKNOWLEDGMENTS

The authors wish to express their gratitude to the staffs of the Van de Graaff accelerator at Université Laval and the McMaster Tandem Accelerator Laboratory for the excellent conditions of the machines, and are indebted to the Natural Sciences and Engineering Research Council of Canada and the OTKA Foundation of the Hungarian Academy of Sciences (No. 1779) for financial support. Discussions with Professor G. E. Mitchell at TUNL are greatly appreciated. We would like to thank Professor G. E. Mitchell for making the code MULTI available to us.

[1] D. C. Kocher and W. Haeberli, Nucl. Phys. **A196**, 225 (1972).
[2] S. Maripuu, Nucl. Phys. **A149**, 593 (1970).
[3] W. R. Wylie, F. Zamboni, and W. Zych, Helv. Phys. Acta **44**, 757 (1971).
[4] J. D. Moses, H. W. Newson, E. G. Bilpuch, and G. E. Mitchell, Nucl. Phys. **A175**, 556 (1971).
[5] G. D. Gunn, J. D. Fox, and G. J. KeKelis, Phys. Rev. C **13**, 595 (1976).
[6] S. Galès, S. Fortier, H. Laurent, L. M. Maison, and J. P.

Schapira, Phys. Rev. C **14**, 842 (1976).
[7] J. P. Schapira, J. M. Maison, M. N. Rao, S. Fortier, S. Galès, and H. Laurent, Phys. Rev. C **17**, 1588 (1978).
[8] I. Fodor, J. Sziklai, P. Kleinwächter, H. Schobbert, and F. Herrmann, J. Phys. G. **5**, 1267 (1979).
[9] I. Fodor and J. Sziklai, Phys. Rev. C **21**, 787 (1980).
[10] P. Kleinwächter, H. U. Gersch, and H. Schobbert, Nucl. Phys. **A398**, 476 (1983).
[11] J. Sziklai, J. A. Cameron, and I. M. Szöghy, Phys. Rev. C **30**, 490 (1984).
[12] J. Sziklai, J. A. Cameron, and I. M. Szöghy, in *Capture Gamma-Ray Spectroscopy and Related Topics*, Knoxville, 1984, Proceedings of the Fifth International Symposium on Capture Gamma-Ray Spectroscopy and Related Topics, AIP Conf. Proc. No. 125, edited by S. Raman (AIP, New York, 1984), p. 688.
[13] Y. Ozawa, Y. Oguri, and E. Arai, Nucl. Phys. **A440**, 13 (1985).
[14] D. Sellin, Ph.D. thesis, Duke University, 1968 (unpublished).
[15] See AIP document No. PAPS-PRVCA-49-686-13 for 13 pages of tables of resonance parameters in ^{52}Cr(p,p_0) and ^{52}Cr(p,p_1) reactions. Order by PAPS number and journal reference from American Institute of Physics, Physics Auxiliary Publication Service, 500 Sunnyside Blvd., Woodbury, New York 11797-2999. The price is $1.50 for each microfiche (60 pages) or $5.00 for photocopies of up to 30 pages, and $0.15 for each additional page over 30 pages. Airmail additional. Make checks payable to the American Institute of Physics.
[16] E. K. Warburton and J. Weneser, in *Isospin in Nuclear Physics*, edited by D. H. Wilkinson (North-Holland, Amsterdam, 1969), p. 174.
[17] M. G. Kendall and A. Stuart, *The Advanced Theory of Statistics* (Hafner, New York, 1961), Vol. 2, Chap. 22.
[18] Y. Baudinet-Robinet, Nucl. Phys. **A222**, 525 (1974).
[19] E. G. Bilpuch, A. M. Lane, G. E. Mitchell, and J. D. Moses, Phys. Rep. **28**, 145 (1976).
[20] H. L. Harney, Computer program HANS, "Calculation of Partial Widths of Isobaric Analog Resonances," Institut de Physique Nucléaire, Orsay, France (1968) (unpublished). This program gives three different results corresponding to the three methods used: (i) W. J. Thompson, J. L. Adams, and D. Robson, Phys. Rev. **173**, 975 (1968), referred to as TAR method; (ii) A. A. A. Zaidi and S. Darmodjo, Phys. Rev. Lett. **19**, 1445 (1967); H. L. Harney, C. A. Wiedner, and J. P. Wurm, Phys. Lett. **26B**, 204 (1968); H. L. Harney, Nucl. Phys. **A119**, 591 (1968), referred to as ZDH method; (iii) A. Mekjian and W. M. MacDonald, Nucl. Phys **A121**, 385 (1968), referred to as MM method.
[21] W. M. MacDonald and A. Z. Mekjian, Phys. Rev. **160**, 730 (1967).
[22] A. K. Kerman and A. F. R. De Toledo Piza, Ann. Phys. (N.Y.) **48**, 183 (1968).
[23] W. M. MacDonald, Ann. Phys. (N.Y.) **125**, 253 (1980).
[24] J. Dubois, Nucl. Phys. **23**, 537 (1961).
[25] A. M. Lane, Ann. Phys. (N.Y.) **63**, 173 (1971).
[26] W. M. MacDonald, Phys. Rev. C **20**, 426 (1979).